

Neural Visibility of Point Sets

JUN-HAO WANG*, Peking University, China
 YI-YANG TIAN*, Peking University, China
 BAOQUAN CHEN, Peking University, China
 PENG-SHUAI WANG[†], Peking University, China

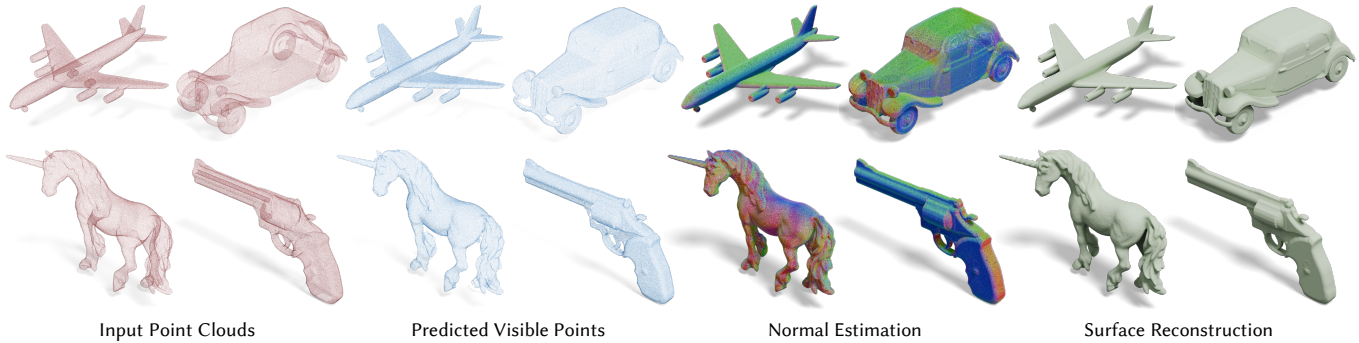


Fig. 1. Our method learns to directly predict the visibility of each point in a point cloud from a given viewpoint. It accurately determines visibility in real time, even in the presence of noise and varying point cloud densities, thereby enabling a wide range of applications. From left to right, the visualizations show the input point clouds, the corresponding predicted visible points from a given viewpoint, the estimated normals based on the predicted visibility, and the final reconstructed meshes using Poisson surface reconstruction.

Point clouds are widely used representations of 3D data, but determining the visibility of points from a given viewpoint remains a challenging problem due to their sparse nature and lack of explicit connectivity. Traditional methods, such as Hidden Point Removal (HPR), face limitations in computational efficiency, robustness to noise, and handling concave regions or low-density point clouds. In this paper, we propose a novel approach to visibility determination in point clouds by formulating it as a binary classification task. The core of our network consists of a 3D U-Net that extracts view-independent point-wise features and a shared multi-layer perceptron (MLP) that predicts point visibility using the extracted features and view direction as inputs. The network is trained end-to-end with ground-truth visibility labels generated from rendered 3D models. Our method significantly outperforms HPR in both accuracy and computational efficiency, achieving up to *126 times* speedup on large point clouds. Additionally, our network demonstrates robustness to noise and varying point cloud densities and generalizes well to unseen shapes. We validate the effectiveness of our approach through extensive experiments on the ShapeNet, ABC Dataset and real-world datasets, showing substantial improvements in visibility accuracy. We also demonstrate the versatility of our method in various applications, including point cloud visualization, surface reconstruction, normal estimation, shadow rendering, and viewpoint optimization. Our code and models are available at <https://github.com/octree-nn/neural-visibility>.

CCS Concepts: • **Computing methodologies** → **Shape analysis; Point-based models; Neural networks.**

*Joint first authors.

[†]Corresponding author.

Authors' Contact Information: Jun-Hao Wang, Wangxuan Institute of Computer Technology, Peking University, China, wangjh24@stu.pku.edu.cn; Yi-Yang Tian, Wangxuan Institute of Computer Technology, Peking University, China; Baoquan Chen, School of Intelligence Science and Technology, Peking University, China; Peng-Shuai Wang, Wangxuan Institute of Computer Technology, Peking University, China, wangps@hotmail.com.

Additional Key Words and Phrases: Point Cloud, Visibility Determination, Octree-based CNNs, Real-time Rendering

1 Introduction

Point clouds are among the most widely used representations of 3D data in computer graphics, computer vision, and robotics. They comprise a set of discrete points in 3D space, possibly augmented with additional attributes such as normals or colors, to capture the geometry and appearance of 3D objects or scenes. However, directly rendering or visualizing point clouds poses challenges, as determining the visibility of points from a given viewpoint is not straightforward and can often be ambiguous.

Mathematically, a point is infinitesimal in size, and the probability of one point being precisely occluded by another from a given viewpoint is nearly zero. A common approach to resolving visibility in point clouds involves reconstructing surfaces from input point clouds [Hoppe et al. 1992; Kazhdan et al. 2006] and performing visibility tests on these reconstructed surfaces. However, surface reconstruction itself remains an open problem [Berger et al. 2017] and is often computationally expensive, particularly for large, noisy, or unoriented point clouds. An alternative line of methods, known as Hidden Points Removal (HPR) [Katz and Tal 2015, 2025; Katz et al. 2007; Mehra et al. 2010], directly determines point visibility without requiring surface reconstruction by transforming the point cloud relative to a sphere centered at the viewpoint and then computing its convex hull. While HPR offers a more direct approach, it is also computationally demanding for large point clouds due to the convex hull computation. Additionally, it performs poorly in the presence of noise, concave regions, or low-density point clouds, limiting its applicability in practical scenarios. There are also methods that project point clouds into pixel space and use neural networks to

predict the visibility of the projected points [Pittaluga et al. 2019; Song et al. 2021]. The accuracy of these methods is often limited by image resolution and point cloud density.

In this paper, we formulate the visibility determination problem in point clouds as a binary classification task and train a neural network to predict the visibility of each point from a given viewpoint. Our key insight is that the visibility of a point cloud is an inherently ill-posed problem without knowledge of the underlying surface. However, we can leverage the power of deep learning to learn the necessary prior information from data, overcoming the limitations of conventional hand-crafted methods like HPR. Given a point cloud, we first extract point-wise features using a 3D U-Net [Ronneberger et al. 2015] built upon octree-based CNNs [Wang et al. 2017]. Subsequently, we employ a lightweight, shared MLP to predict the visibility of each point, taking the extracted point-wise features and viewpoint information as inputs. During training, the whole network is supervised using ground-truth visibility labels generated by rendering the corresponding 3D models from which the point clouds are sampled. Once trained, the network can efficiently extract features for an unseen point cloud in a single forward pass. The visibility of each point is then determined by evaluating the shared MLP, incorporating the viewpoint information.

Our method offers several advantages over existing approaches. First, it is highly efficient and can predict the visibility of point clouds in real-time. The network is readily parallelizable on GPUs, and the extracted point features can be reused across multiple viewpoints. In contrast, the HPR method requires computing a convex hull for each viewpoint, making it less efficient. Second, our network leverages priors learned from data, making it more robust to noise and varying point cloud densities, which enables more accurate visibility predictions in challenging scenarios. Additionally, our method is fully differentiable and can be trained in an end-to-end manner. This property facilitates seamless integration into other optimization or learning pipelines.

We verify the efficiency, effectiveness, and robustness of our method through extensive experiments on the large-scale ShapeNet dataset [Chang et al. 2015] and real-world scans. Specifically, our method consistently outperforms *all* previous approaches, improving visibility accuracy by 1.5% with 81k points and by 3.7% with 2k points on average, and by up to 6.1% in certain categories. Our method also accelerates computation by *126 times* when the number of points is more than *200k* compared to state-of-the-art methods. Moreover, our network demonstrates strong generalization capabilities, performing well on general unseen shapes despite being trained on ShapeNet. We also evaluate our method in various applications, including point cloud visualization, surface reconstruction, normal estimation, shadow casting, and viewpoint optimization. In summary, our contributions are as follows:

- **Novel formulation:** We propose a novel learning-based approach for point cloud visibility determination, addressing limitations of previous methods and possibly inspiring new possibilities for point-based rendering.
- **Efficient design:** Our method uses a 3D U-Net for feature extraction and a lightweight shared MLP for visibility prediction, achieving high efficiency, robustness, and generalization.

- **Effectiveness and extensive applications:** We demonstrate the effectiveness of our method through comprehensive experiments and applications, achieving significant improvements in both visibility accuracy and computational efficiency.

2 Related Work

Visibility Determination. Visibility determination is a fundamental problem in graphics and visualization [Bittner and Wonka 2003; Cohen-Or et al. 2003; Greene et al. 1993; Levvand et al. 2003; Sutherland et al. 1974]. Traditional methods have primarily focused on determining visibility between polygons, whereas our work addresses visibility determination for point clouds, even in the absence of the surfaces they are sampled from. This problem is particularly relevant to point-based rendering. A common approach in point-based rendering involves expanding a point into a surfel or sphere and then splatting it to a Z-buffer [Guennebaud et al. 2004; Rusinkiewicz and Levoy 2000; Zwicker et al. 2001]. However, determining the appropriate radius for the surfel or sphere is challenging, and the process often relies on point normals, which may not be available for all point clouds. Additionally, there are also methods that use neural networks on 2D images to predict the visibility of projected points after projecting the point cloud into pixel space [Pittaluga et al. 2019; Song et al. 2021]. However, the accuracy of these methods is often limited by image resolution and point cloud density, leading to poor generalization performance on different scales of point clouds. In contrast, our approach directly addresses the visibility problem for point clouds without expanding points into surfels or spheres and even without requiring normals. This enables a more general and efficient solution, making it suitable for a wide range of point cloud data.

Surface Reconstruction. After reconstructing the surface from a point cloud, one can determine the visibility with the surface. There exist numerous methods for surface reconstruction from point clouds, with approaches ranging from implicit functions [Carr et al. 2001; Hoppe et al. 1992; Hou et al. 2022; Kazhdan et al. 2006; Kazhdan and Hoppe 2013; Lin et al. 2022; Ohtake et al. 2003], and Moving Least Squares [Alexa et al. 2003; Fleishman et al. 2003], to neural networks [Chen and Zhang 2019; Gropp et al. 2020; Mescheder et al. 2019; Park et al. 2019; Wang et al. 2023]. Despite significant progress, surface reconstruction remains an open challenge; refer to [Berger et al. 2017] for a comprehensive survey. Moreover, surface reconstruction can be computationally intensive in certain scenarios. In contrast, our method directly determines the visibility of point clouds, bypassing the surface reconstruction phase, which is not only more efficient but also well-suited for real-time applications.

Hidden Points Removal. The Hidden Point Removal (HPR) method proposed by [Katz et al. 2007] are the most closely related work. HPR directly determines the visibility of points in a point cloud by transforming the point cloud relative to a sphere centered at the viewpoint and then computing its convex hull. A point is considered visible if it lies on the convex hull. Subsequent works have made efforts to enhance HPR’s performance on noisy and incomplete point clouds [Mehra et al. 2010], analyze the theoretical requirements of the spherical transformation and the properties of HPR [Katz and Tal 2015], improve the efficiency of HPR by using an approximate

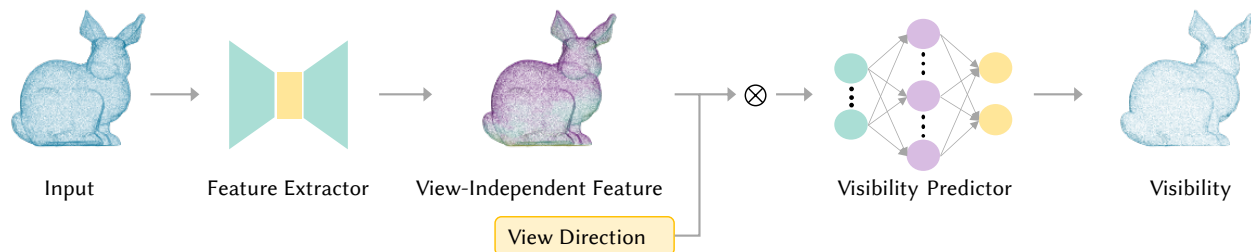


Fig. 2. Overview. The feature extractor is a U-Net that extracts view-independent features from the input point cloud. These extracted features are shared across multiple viewpoints. The view direction is encoded into a high-dimensional space and combined with the extracted features to produce view-dependent features. Finally, a lightweight MLP serves as the visibility predictor, estimating the visibility of each point based on the view-dependent features.

convex hull computation [Silva et al. 2012], and to make HPR differentiable [Katz and Tal 2025]. Despite these improvements, the convex hull computation remains computationally expensive, particularly for large point clouds, while using an approximate convex hull computation can lead to degraded performance. Additionally, HPR struggles with noise and concave regions, limiting its robustness in practical applications. Our method leverages deep neural networks to learn priors from data and directly predict point visibility, which allows for more efficient and accurate visibility determination.

3D Neural Networks. 3D deep learning has made significant advancements in recent years across various applications, including 3D classification, segmentation, reconstruction, and generation. Representative approaches include 3D voxel-based CNNs [Maturana and Scherer 2015; Wu et al. 2015], sparse voxel-based CNNs [Choy et al. 2019; Graham et al. 2018; Wang et al. 2017], and point-based neural networks [Li et al. 2018; Qi et al. 2017a,b]. Recently, transformers have been adapted for 3D data [Engel et al. 2021; Guo et al. 2021; Wang 2023; Wu et al. 2024, 2022; Zhao et al. 2021]. These methods can process point clouds as input, extract point-wise features, and predict point labels. In this paper, we build upon these advancements to tackle the visibility prediction problem of point clouds, presenting a novel application of 3D neural networks.

3 Method

Overview. We formulate visibility determination in point clouds as a learning task and propose a deep neural network to predict point visibility. An overview of our method is shown in Fig. 2. Our network comprises two main components: a powerful feature extractor and a lightweight visibility predictor. The feature extractor is a U-Net [Ronneberger et al. 2015] built upon octree-based CNNs (O-CNN) [Wang et al. 2017], designed to extract view-independent features for each point in the input point cloud. The visibility predictor, implemented as a multi-layer perceptron (MLP), uses these features and the view direction to predict the visibility of each point. For each point cloud, the U-Net performs a single forward pass to extract features, which can then be reused efficiently by the visibility predictor to compute visibility across multiple viewpoints. Unlike prior HPR methods [Katz and Tal 2015; Katz et al. 2007; Mehra et al. 2010] that rely on hand-crafted priors, our approach is data-driven, learning priors directly from data. As a result, our method is not only computationally efficient but also robust to noise, outliers, and

complex concave regions, effectively addressing the limitations of HPR methods. Next, we provide detailed explanations of the feature extractor in Section 3.1, the visibility predictor in Section 3.2, and training data preparation in Section 3.3.

3.1 Feature Extractor

We adopt a U-Net architecture [Ronneberger et al. 2015] built upon O-CNN [Wang et al. 2017] as our feature extractor. The O-CNN is an octree-based sparse 3D convolution framework, demonstrating strong performance across various 3D learning tasks. The architecture of U-Net is illustrated in Fig. 3. It comprises a stack of residual blocks [He et al. 2016], downsampling and upsampling layers, and skip connections. Each residual block contains two octree-based convolutional layers, interleaved with batch normalization [Loffe and Szegedy 2015] and ReLU activation functions.

The feature extractor takes the point cloud as input and outputs a feature vector for each point. Given an input point cloud, we first normalize it to fit within a unit cube and convert it into an octree by recursively subdividing non-empty voxels until the maximum depth is reached. The finest octree nodes contain the average coordinates of the points within each corresponding voxel, which serve as the input signals for the U-Net. If normals are available, we also concatenate the average normals with the average coordinates to form the input signal. The U-Net processes these input signals and produces a feature vector for each octree node at the finest level. To map the features back to the original points, we employ an interpolation module defined on octrees [Yang et al. 2021], which splats the feature vectors to the input points. These point-wise features are then utilized by the visibility predictor to compute visibility. It is important to note that the feature extractor is independent of the viewpoint, allowing the extracted features to be shared across different viewpoints.

3.2 Visibility Predictor

We design a lightweight MLP as the visibility predictor to determine the visibility of each point in the point cloud. The MLP consists of two fully connected layers, with batch normalization and ReLU activation functions. The hidden dimensions of the MLP are set to 128 and 64, respectively. We also experiment with a network with larger hidden dimensions, which converges faster, but the performance improvement is not significant. The input to the MLP consists of the point-wise feature vector extracted by the feature

extractor and the view direction. Visibility determination for each point is formulated as a binary classification task. Therefore, the output layer of the MLP has two channels, representing the scores for visible and invisible, respectively.

The view direction is represented as a unit vector on a 3D sphere. We further encode the view direction using a set of sinusoidal functions [Mildenhall et al. 2020; Tancik et al. 2020] to help the network to learn high-frequency details for the visibility prediction. Let the view direction be represented by a 3D vector $\mathbf{p} = (p_1, p_2, p_3)$. Each component of the view direction is embedded as follows:

$$\gamma(p_i) = \left(\sin(2^0 \pi p_i), \cos(2^0 \pi p_i), \dots, \sin(2^{L-1} \pi p_i), \cos(2^{L-1} \pi p_i) \right),$$

where L denotes the number of frequencies used for encoding the view direction. The three components of \mathbf{p} are embedded separately and then concatenated. We then multiply the embedded view direction by the extracted features from the output of the U-Net to obtain the view-dependent feature, which is subsequently fed into the MLP to predict the visibility of each point. In the experiments, we observed that multiplying these two vectors works slightly better than concatenating them.

For the loss function, we use cross-entropy loss to train the network. The loss is computed as follows:

$$L = -\frac{1}{N} \sum_{i=1}^N y_i \log(\hat{y}_i) + (1 - y_i) \log(1 - \hat{y}_i)$$

where N is the number of points in each training batch, y_i is the ground truth visibility of point i , and \hat{y}_i is the predicted visibility.

3.3 Data Preparation

A remaining challenge is obtaining ground-truth visibility labels for point clouds to train the network. Although freely available 3D datasets such as ShapeNet [Chang et al. 2015] exist, the meshes in these datasets are often of low quality, containing holes or self-intersections, and do not include visibility annotations.

To address this issue, we propose a data preparation scheme to generate synthetic training data with ground-truth visibility labels. We begin by repairing the meshes in ShapeNet to ensure they are watertight and manifold, using the method proposed in [Wang et al. 2022]. Next, we randomly sample 200k points on the surface of the mesh. We randomly and uniformly sample viewpoints on the surface of the bounding sphere of the point cloud. For each point in the point cloud, we connect it to the viewpoint to form a line segment and perform intersection calculations with all triangular faces. If an intersection occurs, the point is considered invisible; otherwise, it is visible. This process is repeated for all points in the point cloud to generate the corresponding visibility labels. Although our network is trained on synthetic data, we demonstrate in Section 4 that it generalizes well to real-world data.

4 Results

In this section, we validate the effectiveness and efficiency of our method through comprehensive evaluations, comparisons, and result analysis in Section 4.1; We showcase a range of applications enabled by our method in Section 4.3.

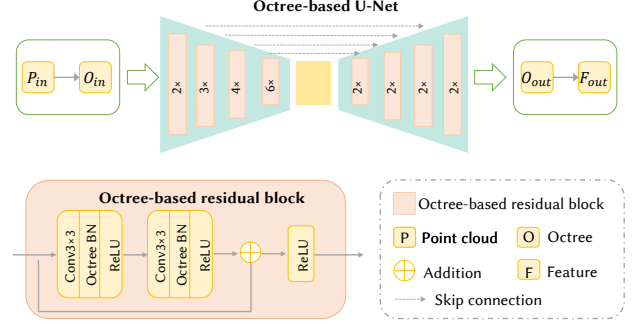


Fig. 3. Feature extractor. The input point cloud is converted into an octree, which serves as the input for feature extraction by a U-Net built upon O-CNN. The symbol $N \times$ in the figure denotes the number of residual blocks within a given stage of the network. The initial channel number in the residual blocks is 32, and the channel number doubles after each downsampling layer while being halved after each upsampling layer.

4.1 Comparisons

In this section, we compare our method with previous approaches to demonstrate its effectiveness, efficiency, scalability, generalization ability, and robustness. Implementation and training details are provided in the supplementary materials.

Comparisons. We compare our method with Hidden Point Removal (HPR) [Katz and Tal 2015; Katz et al. 2007], HPRO [Katz and Tal 2025], and InvSfM [Pittaluga et al. 2019]. We use the visibility accuracy as the evaluation metric following previous works [Katz and Tal 2015, 2025]. We report both the mean accuracy and the per-category accuracy on the ShapeNet test set across four different point densities: 2k, 8k, 32k, and 81k points.

HPR and HPRO require parameter tuning for different point cloud densities. Their performance is sensitive to the choice of the parameter γ , which defines the kernel function for point transformation when determining point visibilities. We tune γ for HPR and HPRO using three groups of parameters and report the best results. However, in real-world applications, it is impractical to fine-tune this parameter for every individual point cloud. InvSfM employs a 2D neural network to predict point visibility in pixel space. We evaluate the pre-trained model provided by the authors using an image resolution of 512, as specified in the original paper. In contrast, our method performs robustly across both sparse and dense point clouds without requiring any parameter tuning in the inference stage.

The quantitative results are presented in Table 1; more detailed results for HPR and HPRO with different parameter settings are provided in the supplementary materials. As shown in Table 1, *our approach outperforms all other methods in nearly all the cases, particularly on sparse point clouds and complex shapes.*

- For dense point clouds with 81k points, our method achieves an average accuracy of 97.4%, outperforming the best existing method by more than 1.5%.
- For sparse point clouds with 2k points, our method achieves an average accuracy of 93.0%, outperforming the best existing method by more than 3.7%.

Table 1. Quantitative comparisons on ShapeNet. The evaluations are conducted on point clouds with 2048, 8192, 32768 and 81920 points, denoted as *2k*, *8k*, *32k* and *81k*, respectively. We report the mean accuracy and per-category accuracy for each method. The last four shaded rows indicate the results of our method when point normals are available, while the other methods cannot utilize point normals as input.

Category	Mean	Airplane	Bag	Bathtub	Bed	Bench	Bottle	Cabinet	Car	Chair	Display	Lamp	Speaker	Pillow	Rifle	Sofa	Table	Phone	Ship
HPR (2k)	89.3	87.9	92.7	88.4	88.0	86.0	94.7	91.1	90.2	87.8	91.1	88.5	92.5	94.6	90.3	92.3	87.5	95.0	90.3
HPRO (2k)	82.3	80.3	84.1	82.0	82.4	80.1	85.5	83.8	86.5	81.9	80.9	80.8	84.5	83.6	80.3	85.0	79.2	81.2	83.1
InvSfM (2k)	39.5	49.8	43.8	35.2	35.7	41.3	38.9	32.3	28.2	41.0	44.6	43.5	32.9	43.8	48.4	38.2	41.2	46.4	40.3
Ours (2k)	93.0	93.6	94.6	91.9	90.6	92.1	94.3	93.4	92.9	91.2	94.4	91.8	92.6	93.3	95.2	95.2	92.8	97.0	93.3
HPR (8k)	93.6	92.3	95.1	93.2	92.8	91.9	97.0	94.7	94.0	92.7	95.0	92.8	95.5	96.6	93.1	95.2	93.2	97.1	93.9
HPRO (8k)	85.6	83.8	86.9	85.3	85.8	84.3	87.4	86.7	89.1	85.7	84.9	83.9	87.2	86.0	83.2	88.0	83.4	84.7	86.1
InvSfM (8k)	52.7	61.0	57.1	51.1	50.1	52.6	54.0	46.0	44.4	55.3	55.4	56.8	46.3	57.6	58.7	51.8	52.8	55.6	54.0
Ours (8k)	96.3	95.9	96.9	97.0	95.4	95.0	97.7	97.8	96.9	95.2	97.1	95.0	97.4	97.4	96.8	97.7	96.1	98.6	96.2
HPR (32k)	95.1	94.6	96.5	94.4	94.1	93.6	97.7	95.3	94.9	94.6	96.2	94.8	96.2	97.2	95.2	96.5	94.8	97.8	95.4
HPRO (32k)	88.6	86.9	89.6	88.2	88.8	88.0	89.3	89.3	91.4	88.9	88.0	86.9	89.6	88.3	85.9	90.5	87.2	87.8	88.8
InvSfM (32k)	65.2	70.3	69.1	65.3	64.4	62.2	69.4	62.8	62.2	67.1	64.8	68.2	64.2	69.0	67.9	64.9	63.1	63.5	66.7
Ours (32k)	97.2	96.7	97.7	98.1	96.5	95.8	98.6	98.7	97.9	96.2	97.8	95.9	98.4	98.4	97.3	98.3	96.8	99.0	97.0
HPR (81k)	96.2	94.7	96.8	96.9	95.8	94.8	98.5	97.1	96.6	95.7	97.1	95.6	97.7	97.9	95.0	97.2	96.2	98.3	96.0
HPRO (81k)	87.7	83.7	87.0	89.4	89.3	87.9	86.9	89.5	92.1	88.3	86.6	84.6	89.4	85.9	81.6	89.1	87.1	84.9	87.2
InvSfM (81k)	70.9	72.3	73.3	71.5	70.4	68.8	75.2	69.3	72.6	72.1	69.4	72.0	71.0	72.8	69.1	70.4	68.3	67.5	73.3
Ours (81k)	97.4	96.8	97.9	98.2	96.7	96.1	98.8	98.8	98.2	96.4	97.8	96.1	98.6	98.6	97.4	98.4	97.0	99.0	97.2
Ours (2k, normal)	97.3	97.3	97.7	98.0	95.5	96.3	99.2	98.3	98.1	96.2	97.7	96.5	98.1	99.2	98.2	98.4	96.6	99.3	97.4
Ours (8k, normal)	97.7	97.4	98.1	98.5	96.6	96.6	99.4	99.0	98.5	96.8	98.1	96.8	98.8	99.4	98.3	98.7	97.2	99.4	97.6
Ours (32k, normal)	97.6	97.1	98.1	98.4	97.0	96.4	99.0	99.0	98.4	96.7	98.2	96.4	98.8	98.9	97.6	98.6	97.2	99.3	97.4
Ours (81k, normal)	97.6	97.1	98.1	98.5	97.0	96.4	99.0	99.0	98.4	96.7	98.2	96.4	98.8	99.0	97.5	98.6	97.2	99.2	97.4

- On complex categories such as *table* and *bench*, our method exceeds the best existing method by over 5.0%.

These results highlight the significant performance improvements of our method, demonstrating its effectiveness and robustness compared to other approaches. Visual comparisons on the ShapeNet dataset are shown in Fig. 5. It can be observed that HPR and HPRO often produce false negatives in regions with high curvature, while InvSfM frequently generates false positives in occluded regions. Our method effectively captures fine geometric details and provides more reliable visibility predictions in challenging regions.

Visibility with Normals. Point normals are available in some real-world point clouds. Our method can be extended to incorporate point normals as additional input features. We report the visibility accuracy of our method under this setting. As shown in the last four rows of Table 1, incorporating normals further boosts our method’s performance, surpassing other methods by a considerable margin. However, the other approaches cannot leverage point normals as input, highlighting a distinct advantage of our method in utilizing additional geometric information for improved accuracy.

Generalization. We design experiments to evaluate the generalization ability of our method on unseen shapes. Specifically, we train the network using only 13 categories from the ShapeNet dataset, as opposed to the 18 categories used in previous experiments, and test it on the remaining 5 categories. All other training settings are kept unchanged. The results are summarized in Table 2. We observe that our method maintains consistent high accuracy on unseen shapes, with only a slight decrease of less than 0.3% compared to training on all 18 categories. This demonstrates the strong generalization capability of our approach in handling unseen shapes. We also report cross-dataset results on the ABC dataset [Koch et al. 2019], using

the model trained on the ShapeNet dataset, as shown in Table 3. The accuracy on the ABC dataset is slightly lower than that on the ShapeNet dataset, likely due to differences in the point cloud distributions between the two datasets. Some point clouds in the ABC dataset contain multiple objects, which our method cannot handle well. Even so, our method achieves accuracies of 89.0% and 92.5% on point clouds with 2k and 81k points, respectively, still outperforming other methods. The results are shown in Fig. 4.

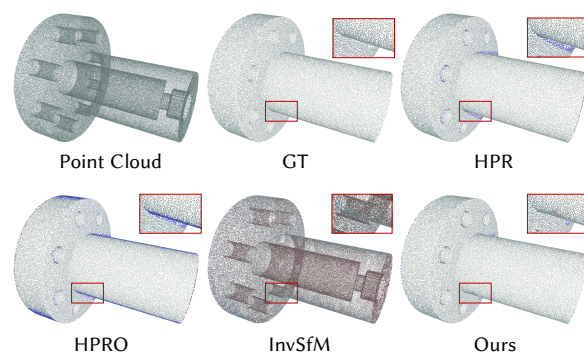


Fig. 4. Results on ABC Dataset.

Scalability. The octree effectively resamples input point clouds, producing approximately consistent features across different sampling densities, thereby ensuring scalability. We train a model on point clouds ranging from 2k to 8k points, and evaluate its performance on point clouds with 16k and 130k points. The results are shown in Fig. 7. The accuracy of our method remains nearly constant as the scale of the point cloud increases, demonstrating

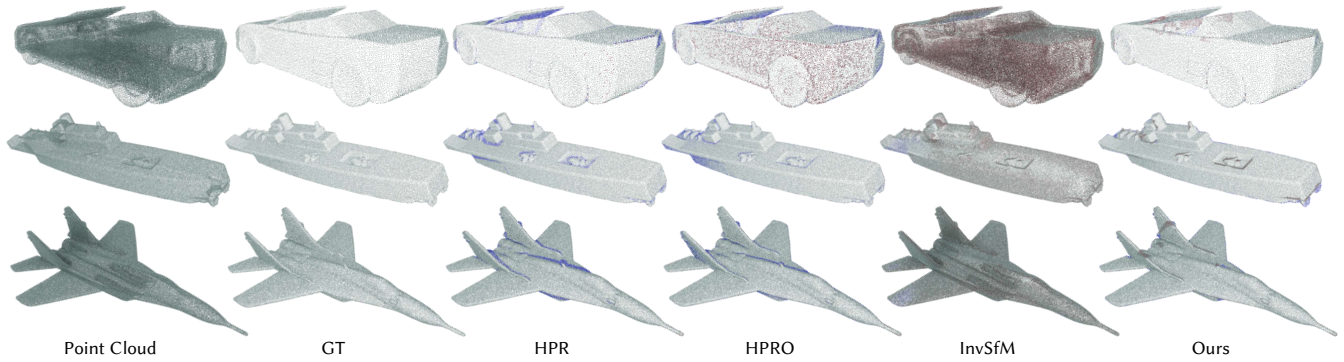


Fig. 5. Results comparisons. From left to right: input point cloud, ground-truth visibility, results from HPR, HPRO, InvSfM, and our method. Each point cloud contains 100k points. Red points indicate false positives, while blue points indicate false negatives. Compared to other methods, our approach produces more accurate visibility predictions, particularly in regions with high curvature.

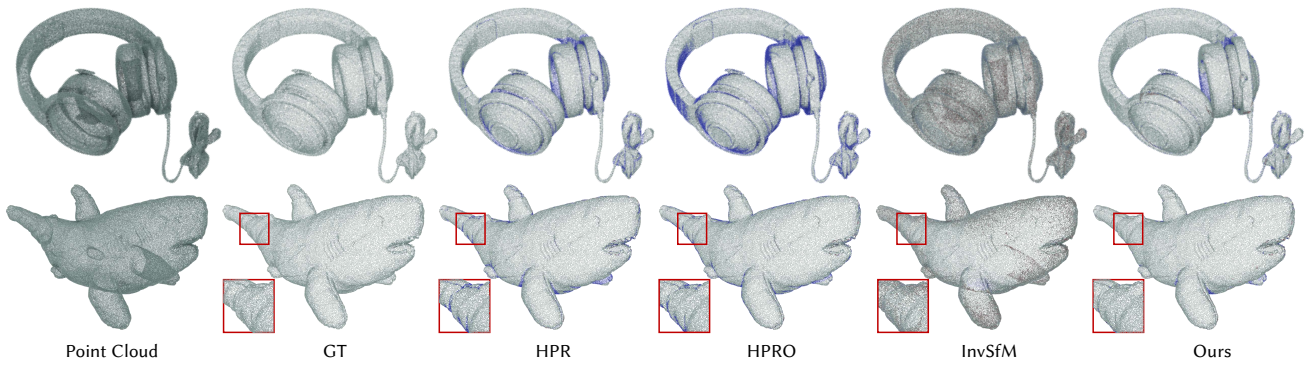


Fig. 6. Results on real-world point clouds. From left to right: input point cloud, ground-truth visibility, results from HPR, HPRO, InvSfM, and our method. Red points indicate false positives, while blue points indicate false negatives.

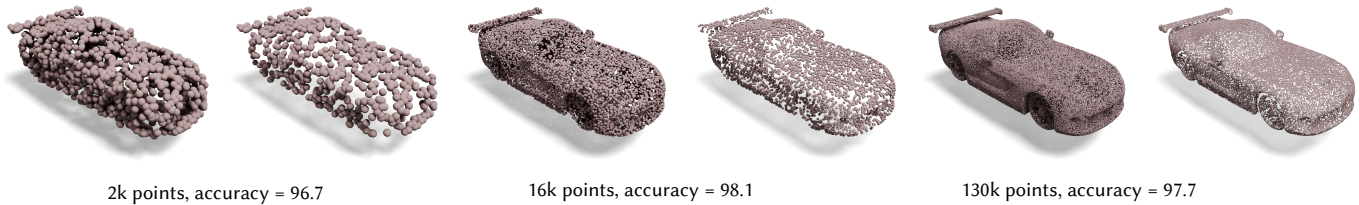


Fig. 7. Scalability. We test our method on point clouds with different scales ranging from 2048 to 130k points, without retraining. Our method demonstrates excellent scalability, with no significant drop in accuracy as the scale increases.

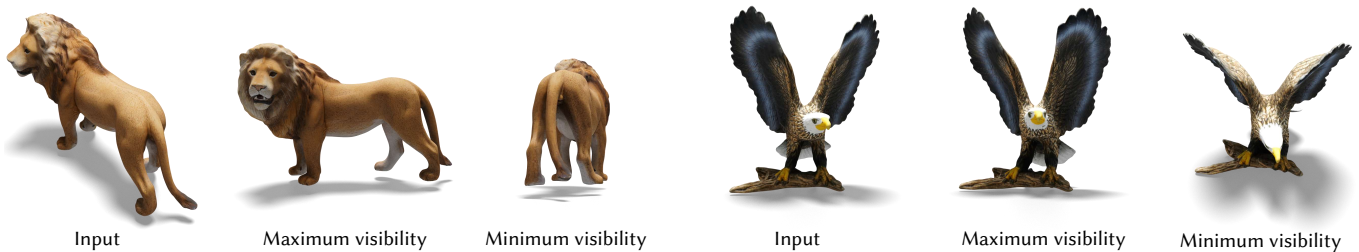


Fig. 8. View optimization. We take the vertices of the mesh as input to extract features with our network, and optimize for 300 iterations to find the maximum and minimum view.

Table 2. Generalization on unseen shapes. *Seen* means these categories are included in the training set, while *Unseen* means these categories were not used during training.

	Bag	Bed	Bottle	Pillow	Phone
Unseen (2k)	94.6	90.4	94.1	93.1	96.9
Seen (2k)	94.6	90.7	94.3	93.2	97.0
Unseen (8k)	96.8	95.3	97.5	97.3	98.5
Seen (8k)	96.9	95.4	97.7	97.4	98.6
Unseen (32k)	97.6	96.5	98.5	98.4	98.9
Seen (32k)	97.7	96.5	98.6	98.4	99.0
Unseen (81k)	97.8	96.7	98.7	98.7	98.9
Seen (81k)	97.9	96.7	98.8	98.7	99.0

Table 3. Accuracy comparisons on the ABC dataset. Our method is trained on the ShapeNet dataset and directly evaluated on the ABC dataset.

Point Number	2k	8k	32k
HPR	88.0	90.5	92.2
HPRO	80.4	83.1	85.6
InvSfM	40.6	46.6	56.1
Ours	89.0	91.7	92.4

Table 4. Robustness. The evaluations are conducted on point clouds with 2048 (2k) and 8192 (8k) points, with noise levels of 1% and 2%. Our method demonstrates strong robustness, consistently outperforming HPR.

Noise Level	1%	2%	Noise Level	1%	2%
HPR (2k)	81.4	79.2	HPR (32k)	84.7	81.3
HPRO (2k)	80.8	78.9	HPRO (32k)	82.6	79.1
InvSfM (2k)	39.2	39.1	InvSfM (32k)	64.1	62.7
Ours (2k)	88.9	87.8	Ours (32k)	93.3	91.4
HPR (8k)	83.6	80.8	HPR (81k)	83.5	79.3
HPRO (8k)	82.3	79.5	HPRO (81k)	79.5	76.0
InvSfM (8k)	52.1	51.6	InvSfM (81k)	69.7	68.0
Ours (8k)	91.8	90.4	Ours (81k)	94.0	91.6

excellent scalability. This property is particularly advantageous for real-world applications, where point clouds often vary in size and density. However, HPR and HPRO require manual parameter tuning to accommodate different point densities, and InvSfM is also sensitive to the number of points in the point cloud.

Robustness. We evaluate the robustness of our method on noisy and incomplete point clouds. For noisy point clouds, we add uniformly distributed noise of varying magnitudes to each point, following the approach in [Mehra et al. 2010]. Specifically, we train our network on point clouds with 2% noise and evaluate its performance on point clouds with noise levels of 1% and 2%. The noise level refers to the upper bound of the noise magnitude, expressed as a percentage of the bounding box size. The results are presented in Table 4. Our method demonstrates strong robustness to noise, outperforming other approaches by more than 7% in accuracy across both noise levels. Visual results are shown in Fig. 9. Compared to other methods, our approach effectively reduces both false positives and false negatives, particularly at higher noise levels.

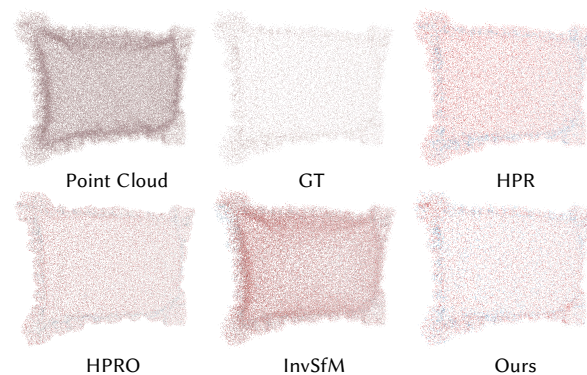


Fig. 9. Results on noisy point clouds. The noise levels is 0.01. The red and blue points represent the false positives and false negatives, respectively. Our method significantly improves the accuracy, demonstrating its robustness.

For incomplete point clouds, we randomly select three viewpoints and remove points that are not visible from any of them. We directly apply the model trained on complete point clouds to these incomplete inputs. As shown in Fig. 10, even with incomplete point clouds, our method accurately predicts point visibility. This indicates that our method effectively learns shape priors from the training data, enabling it to generalize well to incomplete data.

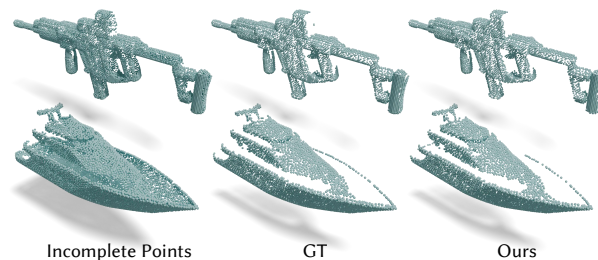


Fig. 10. Results on incomplete point clouds. Our model is trained on ShapeNet, it can accurately predict the visibility for incomplete point clouds.

Efficiency. One of the key advantages of our method is its efficiency. The HPR method requires constructing a convex hull for each viewpoint, with an average time complexity of $O(n \log n)$ and a worst-case complexity of $O(n^2)$, where n is the number of points in the point cloud. The Efficient HPR method [Silva et al. 2012] improves upon this by leveraging a GPU-based implementation to approximate the convex hull, reducing the average time complexity to $O(n \log n/m)$, where m depends on the number of GPU cores. In contrast, our method computes visibility through a simple feed-forward pass of a lightweight two-layer MLP after extracting features from the point cloud with the octree-based U-Net. As a result, the time complexity of our method is effectively $O(n/m)$.

The comparison of time consumption for point clouds of varying sizes is presented in Fig. 11. As the number of points increases, the inference time of our visibility predictor (the MLP) grows approximately linearly beyond 50k points. Meanwhile, the time required for the feature extractor (the U-Net) converges to a constant, as the

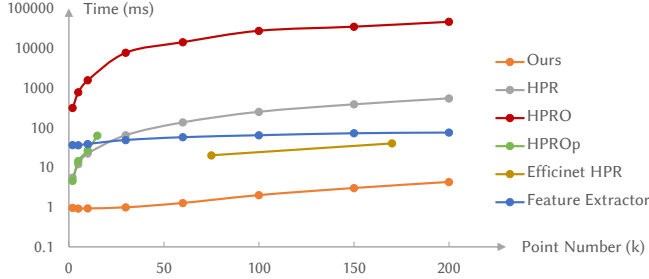


Fig. 11. Efficiency comparison. HPROp is a parallel implementation of HPRO with significantly higher memory usage. With 24GB of memory, we can only test it on point clouds containing up to 15k points. The results of Efficient HPR is from [Silva et al. 2012]. Feature Extractor is the time consumption of our U-Net, which is forwarded once for each point cloud.

Table 5. Effects of the octree depth. The first row presents the time consumption of the feature extractor in milliseconds, the second row shows the corresponding accuracy.

Depth	6	7	8	9
Time	30.7	35.6	49.3	75.0
Accuracy	95.7	97.1	97.4	97.3

number of nodes in the octree is bounded by its maximum depth. The preprocessing time of our feature extractor (the U-Net) is 75ms for 200k points on single L40 GPU with memory cost less than 5GB, which is forwarded once for each point cloud, still much faster than HPR. When the point cloud exceeds 200k points, our method significantly outperforms the HPR method, achieving a speedup of up to 126 times. Specifically, our method processes a point cloud of this size in just 4.27 ms, compared to 541.5 ms for HPR.

Real-world Point Clouds. We evaluate our method on real-world point clouds from the Google Scanned Objects dataset [Downs et al. 2022]. The results are shown in Fig. 6. These real-world point clouds exhibit significantly greater geometric complexity than those in the ShapeNet dataset. Despite being trained solely on ShapeNet, our method generates accurate visibility predictions on these real-world examples, demonstrating strong robustness and generalization capabilities. Compared to HPR, our approach consistently achieves better performance, particularly in high-curvature regions, highlighting its effectiveness in handling complex and diverse shapes.

4.2 Ablation Study and Discussions

In this section, we conduct ablation studies to analyze the impact of key design choices in our model.

Octree Depth. We evaluate the effect of octree depth on the performance and efficiency on the ShapeNet dataset. The results are summarized in Table 5. A small octree depth leads to a coarse representation of the point cloud, which may result in a loss of important geometric details, while a large octree depth increases the computational cost of extracting features. In our experiments, we set the

Table 6. Comparisons with transformer-based feature extractor. OctFormer performs similarly to OCNN-based U-Net.

Point Number	2k	8k	32k	81k
OCNN	93.0	96.3	97.2	97.4
Octformer	93.8	96.4	97.0	97.1

Table 7. Ablation study on position embedding and U-Net architecture.

Point Number	2k	8k	32k	81k
w/o position embedding	92.3	95.7	96.7	96.9
5-layer Unet	93.0	96.3	97.2	97.4
Ours	93.0	96.3	97.2	97.4



Fig. 12. Failure cases on ShapeNet.

octree depth to 8, which provides a good balance between accuracy and efficiency.

Transformer-based Feature Extractor. Transformers are generally considered more effective at capturing global relationships. To evaluate their performance in our task, we replaced the OCNN-based feature extractor with OctFormer [Wang 2023]. The results are presented in Table 6. The accuracy difference between the two architectures does not exceed 1%. This suggests that the CNN-based U-Net has sufficient capacity to capture global context for the visibility prediction task.

Position Embedding and Unet Architecture. We evaluate the effect of position embedding and the U-Net architecture on the performance of our method. As shown in Table 7, using position embedding improves the performance of our method by 0.5% on average, from 96.9% to 97.4% on the ShapeNet dataset. As for the U-Net architecture, We tested a deeper U-Net (5 layers), which increased the parameter count from 40 M to 130 M, yet the test accuracy remained the same, which is identical to the current result.

Additional Metrics. We computed the false-negative/positive rates on ShapeNet, measuring the proportions of visible points predicted as invisible, and vice versa. Our method achieved 4.3% and 2.0%, respectively, compared to HPR’s 9.2% and 1.1%. Notably, our false-negative rate is 4.9% lower than HPR’s.

Failure cases. Our method sometimes encounters failure cases on thin structures, large curvature concave surfaces, and multi-layer occlusions. Some examples are shown in Fig. 12. This may require improvement on the network or the training strategy.

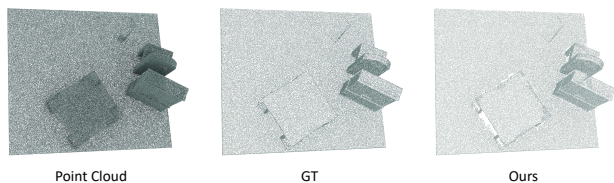


Fig. 13. Results on scene-level point clouds. Left: input point clouds. Right: visible points predicted by our method.

Scene-level Results. We evaluate our model on a scene dataset composed of multiple ShapeNet objects [Peng et al. 2020], with 500 training and 125 testing scenes. Using the ShapeNet-trained model, we achieve 94.3% accuracy. Fine-tuning on the scene dataset further improves accuracy to 95.1%. Results are shown in Fig. 13. Our method performs slightly worse in predicting occlusions between objects, which still requires further improvement.

4.3 Applications

In this section, we showcase a range of applications enabled by our method, including point cloud visualization, best view selection, view-dependent surface reconstruction, normal estimation, and shadow casting.

Point Cloud Visualization. A direct application of our method is point cloud visualization. By rendering only the visible points, our approach effectively removes occluded regions, resulting in a clear and informative representation of the shape. This is particularly advantageous for point clouds containing color or normal information, as it significantly enhances the clarity and interpretability of the rendering results. Several examples are shown in Fig. 14.

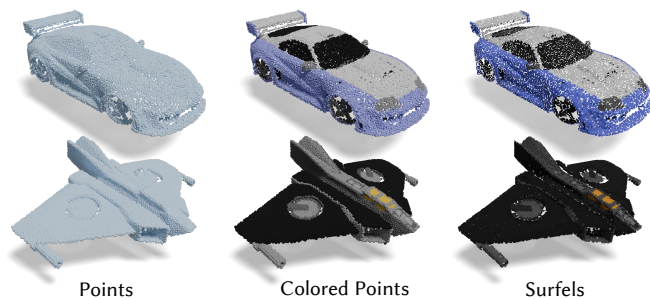


Fig. 14. Point cloud visualization. The left column shows the results of our method, while the middle and right columns are rendered with color and surfels, respectively.

View-dependent Surface Reconstruction. Our method enables surface reconstruction of a 3D shape from a point cloud, even in the absence of point normals. After determining the visibility of each point, we project the visible points into the view space and apply Delaunay triangulation to establish the connectivity among points. The resulting triangulation is then mapped back to 3D to generate a view-dependent mesh. To maintain the visual coherence of the reconstructed surface, we discard triangles whose edge lengths exceed a predefined threshold. The results are presented in Fig. 15.



Fig. 15. View-dependent Surface Reconstruction.

Normal Estimation. Following view-dependent surface reconstruction, we can estimate the normal of each point by averaging the normals of the triangles that contain it. We uniformly sample 26 viewpoints around the point cloud and compute the average of the normal estimations across these views. For points that are not visible from any of the sampled views, we propagate the normal from the nearest visible point. The comparison results are shown in Table 8. Using the resulting predicted normals, we perform surface reconstruction via Poisson surface reconstruction [Kazhdan et al. 2006]. The results are presented in Fig. 16 and the quantitative results are presented in Table 9.



Fig. 16. Normal estimation and reconstruction. We predict and aggregate the normals from 26 fixed viewpoints, then reconstruct the surface by Poisson surface reconstruction. The cosine similarity between the predicted normals and the ground truth normals is all above 0.93.

Shadow Casting. Shadow casting is essential for enhancing the realism of 3D scenes in computer graphics [Hasenfratz et al. 2003]. Using our method, shadows can be seamlessly incorporated into

Table 8. Quantitative pointcloud normal prediction result comparison between PCPNet [Guerreiro et al. 2017] and our method. We tested using three sets of data: PCPNet’s test data (from its provided dataset) **A**, our test data (from the ShapeNet dataset) **B**, and test data unseen during training (from the COSEG dataset) **C**.

Dataset	Method	Mean Radian Error	Mean Angle Error
A	PCPNet	0.156	6.63
A	Ours	0.156	9.14
B	PCPNet	0.126	7.23
B	Ours	0.062	3.55
C	PCPNet	0.085	4.84
C	Ours	0.059	3.39

Table 9. Quantitative mesh surface reconstruction accuracy results conducted on a non-training dataset(COSEG).

Category	Chamfer Distance	Hausdorff Distance	F1-score
Chairs	5×10^{-5}	0.0228	1.000
Fourleg	7×10^{-5}	0.0241	1.000
Guitars	5×10^{-5}	0.0182	0.999
Lamps	5×10^{-5}	0.0166	1.000

point clouds. To render shadows, we treat the light source as the viewpoint and determine shadowed and illuminated regions using a z-buffer in object space. Our approach predicts the visible points directly from the perspective of the light source. We then construct the connectivity of these visible points using Delaunay triangulation. By interpolating their depth values, we generate a depth map from the light source’s perspective, which serves as a shadow map for rendering. This process enables accurate identification and rendering of shadowed regions. The results are shown in Fig. 17.

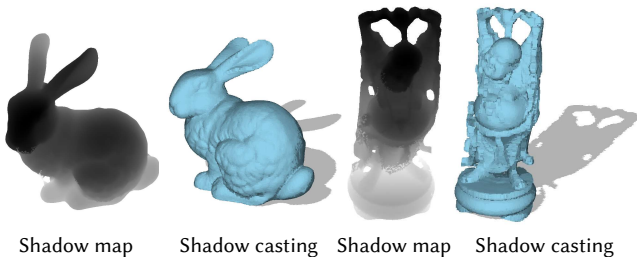


Fig. 17. Shadow casting. The first and third images show the depth map under the light source, which are used as the shadow maps. The second and fourth images show the rendering results with shadows.

View Selection. View selection is an important problem in computer graphics and visualization [Leifman et al. 2016]. As our approach is differentiable, we can optimize the viewpoint directly by minimizing the invisibility score of the point cloud defined as:

$$\mathcal{L}(v) = \frac{1}{N} \sum_{i=1}^N o_i(v),$$

where v is the viewpoint, $o_i(v)$ is the invisibility score predicted by the network for the i -th point, and N is the total number of points

in the point cloud. By minimizing this loss while keeping the network parameters fixed, we can effectively identify a viewpoint that maximizes visible details and minimizes occlusions, resulting in a more comprehensive view of the shape. Conversely, by maximizing the invisibility score, we can determine the viewpoint that yields the least visible details. The results are shown in Fig. 8, and the loss curve during optimization is presented in Fig. 18.

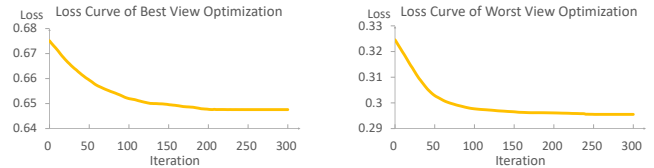


Fig. 18. Loss curve of best and worst view optimization.

5 Conclusions

This paper introduces a novel approach for visibility determination in point clouds by framing the problem as a learning task. Utilizing an octree-based U-Net for feature extraction and a shared multi-layer perceptron (MLP) for visibility prediction, our method offers significant improvements over traditional techniques in both accuracy and computational efficiency. Extensive experiments on ShapeNet and real-world datasets demonstrate the robustness and generalization capabilities of our method. Moreover, our method supports a variety of applications, including surface reconstruction, normal estimation, shadow casting, and viewpoint optimization. We hope that our work will inspire future research in visibility determination and facilitate the development of more efficient and robust methods for point-based rendering and point cloud processing.

Despite these advancements, there are several limitations and future works for improvements. First, our model focuses on single objects with viewpoints located outside the visual hull. Extending it to handle scene-level visibility prediction or multi-object scenarios would be a valuable direction for future research. Second, our method relies on ground-truth visibility labels for training, which may not always be available in real-world scenarios. Future work could explore semi-supervised or self-supervised learning strategies to reduce dependency on labeled data. Third, to better capture partial occlusions or transparency effects, extending our approach to model probabilistic visibility rather than binary visibility is a promising avenue. Finally, incorporating additional data augmentation techniques and large-scale training strategies could further enhance generalization, especially in complex real-world settings.

Acknowledgments

This work was supported in part by National Natural Science Foundation of China (Grant No. 62371409) and Beijing Natural Science Foundation (Grant No. 4244081). We also thank the anonymous reviewers for their invaluable feedback.

References

- Marc Alexa, Johannes Behr, Daniel Cohen-Or, Shachar Fleishman, David Levin, and Claudio T. Silva. 2003. Computing and rendering point set surfaces. *IEEE. T. Vis. Comput. Gr.* 9, 1 (2003).
- Matthew Berger, Andrea Tagliasacchi, Lee M. Seversky, Pierre Alliez, Gaël Guennebaud, Joshua A. Levine, Andrei Sharf, and Claudio T. Silva. 2017. A survey of surface reconstruction from point clouds. *Comput. Graph. Forum* 36, 1 (2017).
- Jiri Bittner and Peter Wonka. 2003. Visibility in computer graphics. *Environment and Planning B: Planning and Design* 30, 5 (2003).
- Jonathan C Carr, Richard K Beatson, Jon B Cherrie, Tim J Mitchell, W Richard Fright, Bruce C McCallum, and Tim R Evans. 2001. Reconstruction and representation of 3D objects with radial basis functions. In *SIGGRAPH*.
- Angel X. Chang, Thomas Funkhouser, Leonidas J. Guibas, Pat Hanrahan, Qixing Huang, Zimo Li, Silvio Savarese, Manolis Savva, Shuran Song, Hao Su, Jianxiong Xiao, Li Yi, and Fisher Yu. 2015. ShapeNet: An information-rich 3D model repository. *arXiv preprint arXiv:1512.03012* (2015).
- Zhiqin Chen and Hao Zhang. 2019. Learning implicit fields for generative shape modeling. In *CVPR*.
- Christopher Choy, JunYoung Gwak, and Silvio Savarese. 2019. 4D spatio-temporal convnets: Minkowski convolutional neural networks. In *CVPR*.
- Daniel Cohen-Or, Yiorgos L Chrysanthou, Claudio T. Silva, and Frédo Durand. 2003. A survey of visibility for walkthrough applications. *IEEE. T. Vis. Comput. Gr.* 9, 3 (2003).
- Laura Downs, Anthony Francis, Nate Koenig, Brandon Kinman, Ryan Hickman, Krista Reymann, Thomas B McHugh, and Vincent Vanhoucke. 2022. Google Scanned Objects: A high-quality dataset of 3D scanned household items. In *ICRA*.
- Nico Engel, Vasileios Belagiannis, and Klaus Dietmayer. 2021. Point transformer. *IEEE Access* 9 (2021).
- Shachar Fleishman, Daniel Cohen-Or, Marc Alexa, and Claudio T Silva. 2003. Progressive point set surfaces. *ACM Trans. Graph. (SIGGRAPH)* 22, 4 (2003).
- Benjamin Graham, Martin Engelcke, and Laurens van der Maaten. 2018. 3D semantic segmentation with submanifold sparse convolutional networks. In *CVPR*.
- Ned Greene, Michael Kass, and Gavin Miller. 1993. Hierarchical Z-buffer visibility. In *SIGGRAPH*.
- Amos Gropp, Lior Yariv, Niv Haim, Matan Atzmon, and Yaron Lipman. 2020. Implicit geometric regularization for learning shapes. In *ICML*.
- Gael Guennebaud, Loïc Barthe, and Mathias Paulin. 2004. Deferred splatting. In *Comput. Graph. Forum*, Vol. 23.
- Paul Guerrero, Yanir Kleiman, Maks Ovsjanikov, and Niloy J. Mitra. 2017. PCPNET: Learning Local Shape Properties from Raw Point Clouds. *CoRR* abs/1710.04954 (2017).
- Meng-Hao Guo, Jun-Xiong Cai, Zheng-Ning Liu, Tai-Jiang Mu, Ralph R Martin, and Shi-Min Hu. 2021. PCT: Point cloud transformer. *Comput. Vis. Media* 7, 2 (2021).
- Jean-Marc Hasenfratz, Marc Lapierre, Nicolas Holzschuch, and François X Sillion. 2003. A survey of real-time soft shadows algorithms. In *Comput. Graph. Forum*, Vol. 22.
- Kaiming He, Xiangyu Zhang, Shaoqing Ren, and Jian Sun. 2016. Deep residual learning for image recognition. In *CVPR*.
- Hugues Hoppe, Tony DeRose, John McDonald, and Werner Stuetzle. 1992. Surface reconstruction from unorganized points. In *SIGGRAPH*.
- Fei Hou, Chiyu Wang, Wencheng Wang, Hong Qin, Chen Qian, and Ying He. 2022. Iterative poisson surface reconstruction (IPSR) for unoriented points. *ACM Trans. Graph. (SIGGRAPH)* 41, 4 (2022).
- Sagi Katz and Ayellet Tal. 2015. On the visibility of point clouds. In *CVPR*.
- Sagi Katz and Ayellet Tal. 2025. HPRO: Direct Visibility of Point Clouds for Optimization. *Comput. Graph. Forum (EG)*.
- Sagi Katz, Ayellet Tal, and Ronen Basri. 2007. Direct visibility of point sets. In *SIGGRAPH*.
- Michael Kazhdan, Matthew Bolitho, and Hugues Hoppe. 2006. Poisson surface reconstruction. In *Symp. Geom. Proc.*
- Michael Kazhdan and Hugues Hoppe. 2013. Screened Poisson surface reconstruction. *ACM Trans. Graph.* 32, 3 (2013).
- Sebastian Koch, Albert Matveev, Zhongshi Jiang, Francis Williams, Alexey Artemov, Evgeny Burnaev, Marc Alexa, Denis Zorin, and Daniele Panozzo. 2019. ABC: A big CAD model dataset for geometric deep learning. In *CVPR*.
- George Leifman, Elizabeth Shtrom, and Ayellet Tal. 2016. Surface regions of interest for viewpoint selection. *IEEE Trans. Pattern Anal. Mach. Intell.* 38, 12 (2016).
- Tommer Leyvand, Olga Sorkine, and Daniel Cohen-Or. 2003. Ray space factorization for from-region visibility. In *SIGGRAPH*.
- Yangyan Li, Rui Bu, Mingchao Sun, Wei Wu, Xinhan Di, and Baoquan Chen. 2018. PointCNN: Convolution on X-transformed points. In *NeurIPS*.
- Siyu Lin, Dong Xiao, Zuoqiang Shi, and Bin Wang. 2022. Surface Reconstruction from Point Clouds without Normals by Parametrizing the Gauss Formula. *ACM Trans. Graph.* 42, 2 (2022).
- Sergey Lofte and Christian Szegedy. 2015. Batch Normalization: Accelerating deep network training by reducing internal covariate shift. In *ICML*.
- Daniel Maturana and Sebastian Scherer. 2015. VoxNet: A 3D convolutional neural network for real-time object recognition. In *ROS*.
- Ravish Mehra, Pushkar Tripathi, Alla Sheffer, and Niloy J. Mitra. 2010. Visibility of noisy point cloud data. *Computers & Graphics* 34, 3 (2010).
- Lars Mescheder, Michael Oechsle, Michael Niemeyer, Sebastian Nowozin, and Andreas Geiger. 2019. Occupancy networks: Learning 3D reconstruction in function space. In *CVPR*.
- Ben Mildenhall, Pratul P Srinivasan, Matthew Tancik, Jonathan T Barron, Ravi Ramamoorthi, and Ren Ng. 2020. NeRF: Representing scenes as neural radiance fields for view synthesis. In *ECCV*.
- Yutaka Ohtake, Alexander Belyaev, Marc Alexa, Greg Turk, and Hans-Peter Seidel. 2003. Multi-level partition of unity implicits. *ACM Trans. Graph. (SIGGRAPH)* 22, 3 (2003).
- Jeong Joon Park, Peter Florence, Julian Straub, Richard Newcombe, and Steven Lovegrove. 2019. DeepSDF: Learning continuous signed distance functions for shape representation. In *CVPR*.
- Songyou Peng, Michael Niemeyer, Lars Mescheder, Marc Pollefeys, and Andreas Geiger. 2020. Convolutional occupancy networks. In *ECCV*.
- Francesco Pittaluga, Sanjeev J Koppal, Sing Bing Kang, and Sudipta N Sinha. 2019. Revealing scenes by inverting structure from motion reconstructions. In *CVPR*.
- Charles R. Qi, Hao Su, Kaichun Mo, and Leonidas J. Guibas. 2017a. PointNet: Deep learning on point sets for 3D classification and segmentation. In *CVPR*.
- Charles R. Qi, Li Yi, Hao Su, and Leonidas J. Guibas. 2017b. PointNet++: Deep hierarchical feature learning on point sets in a metric space. In *NeurIPS*.
- Olaf Ronneberger, Philipp Fischer, and Thomas Brox. 2015. U-Net: Convolutional networks for biomedical image segmentation. In *International Conference on Medical image computing and computer-assisted intervention*.
- Szymon Rusinkiewicz and Marc Levoy. 2000. QSplat: A multiresolution point rendering system for large meshes. In *SIGGRAPH*.
- Renan Machado e Silva, Claudio Esperança, and Antonio Oliveira. 2012. Efficient HPR-based rendering of point clouds. In *SIBGRAPI Conference on Graphics, Patterns and Images*.
- Shuang Song, Zhaopeng Cui, and Rongjun Qin. 2021. Vis2mesh: Efficient mesh reconstruction from unstructured point clouds of large scenes with learned virtual view visibility. In *ICCV*.
- Ivan E Sutherland, Robert F Sproull, and Robert A Schumacker. 1974. A characterization of ten hidden-surface algorithms. *ACM Computing Surveys (CSUR)* (1974).
- Matthew Tancik, Pratul P. Srinivasan, Ben Mildenhall, Sara Fridovich-Keil, Nithin Raghavan, Utkarsh Singhal, Ravi Ramamoorthi, Jonathan T. Barron, and Ren Ng. 2020. Fourier Features Let Networks Learn High Frequency Functions in Low Dimensional Domains. In *NeurIPS*.
- Peng-Shuai Wang. 2023. OctFormer: Octree-based Transformers for 3D Point Clouds. *ACM Trans. Graph. (SIGGRAPH)* 42, 4 (2023).
- Peng-Shuai Wang, Yang Liu, Yu-Xiao Guo, Chun-Yu Sun, and Xin Tong. 2017. O-CNN: Octree-based convolutional neural networks for 3D shape analysis. *ACM Trans. Graph. (SIGGRAPH)* 36, 4 (2017).
- Peng-Shuai Wang, Yang Liu, and Xin Tong. 2022. Dual Octree Graph Networks for Learning Adaptive Volumetric Shape Representations. *ACM Trans. Graph. (SIGGRAPH)* 41, 4 (2022).
- Zixiong Wang, Yunxiao Zhang, Rui Xu, Fan Zhang, Peng-Shuai Wang, Shuangmin Chen, Shiqing Xin, Wenping Wang, and Changhe Tu. 2023. Neural-Singular-Hessian: Implicit Neural Representation of Unoriented Point Clouds by Enforcing Singular Hessian. *ACM Trans. Graph. (SIGGRAPH ASIA)* 42, 6 (2023).
- Xiaoyang Wu, Li Jiang, Peng-Shuai Wang, Zhijian Liu, Xihui Liu, Yu Qiao, Wanli Ouyang, Tong He, and Hengshuang Zhao. 2024. Point Transformer V3: Simpler Faster Stronger. In *CVPR*.
- Xiaoyang Wu, Yixing Lao, Li Jiang, Xihui Liu, and Hengshuang Zhao. 2022. Point Transformer V2: Grouped Vector Attention and Partition-based Pooling. In *NeurIPS*.
- Zhirong Wu, Shuran Song, Aditya Khosla, Fisher Yu, Linguang Zhang, Xiaoou Tang, and Jianxiong Xiao. 2015. 3D ShapeNets: A deep representation for volumetric shape modeling. In *CVPR*.
- Yu-Qi Yang, Peng-Shuai Wang, and Yang Liu. 2021. Interpolation-aware padding for 3D sparse convolutional neural networks. In *ICCV*.
- Hengshuang Zhao, Li Jiang, Jiaya Jia, Philip Torr, and Vladlen Koltun. 2021. Point transformer. In *ICCV*.
- Matthias Zwicker, Hanspeter Pfister, Jeroen Van Baar, and Markus Gross. 2001. Surface splatting. In *SIGGRAPH*.